The Astrophysical Journal, 944:208 (12pp), 2023 February 20 https://doi.org/10.3847/1538-4357/acb5e8

Cyanopolyyne Chemistry in the L1544 Prestellar Core: New Insights from GBT Observations

Eleonora Bianchi[1,2,3,4], Anthony Remijan[5], Claudio Codella[4,3], Cecilia Ceccarelli[3], Francois Lique[6], Silvia Spezzano[7], Nadia Balucani[8,4], Paola Caselli[7], Eric Herbst[9,10], Linda Podio[4], Charlotte Vastel[11], and Brett McGuire[12,5]

[1] Excellence Cluster ORIGINS, Boltzmannstraße 2, D-85748 Garching bei München, Germany; eleonora.bianchi@origins-cluster.de
[2] Ludwig-Maximilians-Universität, Schellingstraße 4, D-80799 München, Germany
[3] Univ. Grenoble Alpes, CNRS, IPAG, F-38000 Grenoble, France
[4] INAF, Osservatorio Astrofisico di Arcetri, Largo E. Fermi 5, I-50125, Firenze, Italy
[5] National Radio Astronomy Observatory, Charlottesville, VA 22903, USA
[6] Univ. Rennes, CNRS, IPR [(Institut de Physique de Rennes)] - UMR 6251, F-35000 Rennes, France
[7] Max-Planck-Institut für extraterrestrische Physik (MPE), Giessenbachstrasse 1, D-85748 Garching, Germany
[8] Dipartimento di Chimica, Biologia e Biotecnologie, Via Elce di Sotto 8, I-06123 Perugia, Italy
[9] Department of Chemistry, University of Virginia, Charlottesville, VA 22904, USA
[10] Department of Astronomy, University of Virginia, Charlottesville, VA 22904, USA
[11] IRAP, Université de Toulouse, CNRS, UPS, CNES, F-31400 Toulouse, France
[12] Department of Chemistry, Massachusetts Institute of Technology, Cambridge, MA 02139, USA
Received 2022 October 25; revised 2023 January 23; accepted 2023 January 23; published 2023 February 27

Abstract

We report a comprehensive study of the cyanopolyyne chemistry in the prototypical prestellar core L1544. Using the 100 m Robert C. Byrd Green Bank Telescope, we observe three emission lines of HC_3N, nine lines of HC_5N, five lines of HC_7N, and nine lines of HC_9N. HC_9N is detected for the first time toward the source. The high spectral resolution ($\sim$0.05 km s^{-1}) reveals double-peak spectral line profiles with the redshifted peak a factor 3–5 brighter. Resolved maps of the core in other molecular tracers indicate that the southern region is redshifted. Therefore, the bulk of the cyanopolyyne emission is likely associated with the southern region of the core, where free carbon atoms are available to form long chains, thanks to the more efficient illumination of the interstellar field radiation. We perform a simultaneous modeling of the HC_5N, HC_7N, and HC_9N lines to investigate the origin of the emission. To enable this analysis, we performed new calculation of the collisional coefficients. The simultaneous fitting indicates a gas kinetic temperature of 5–12 K, a source size of 80″, and a gas density larger than 100 cm^{-3}. The HC_5N:HC_7N:HC_9N abundance ratios measured in L1544 are about 1:6:4. We compare our observations with those toward the well-studied starless core TMC-1 and with the available measurements in different star-forming regions. The comparison suggests that a complex carbon chain chemistry is active in other sources and is related to the presence of free gaseous carbon. Finally, we discuss the possible formation and destruction routes in light of the new observations.

Unified Astronomy Thesaurus concepts: Astrochemistry (75); Star formation (1569); Interstellar medium (847); Interstellar molecules (849); Chemical abundances (224)

1. Introduction

The formation of a solar-type planetary system starts with the collapse of a cold ($\leqslant$10 K) and dense ($\geqslant 10^5$ cm^{-3}) core, called a prestellar core, in a molecular cloud. The evolution of the prestellar core into a protostar, a protoplanetary disk, and, eventually, a planetary system is also accompanied by the evolution of its chemical composition (e.g., Caselli & Ceccarelli 2012).

Cyanopolyynes are a class of molecules composed of a long chain of carbon atoms with a hydrogen atom at one end and a cyanide (CN) group at the other end. They are widespread in the interstellar medium (ISM), and they have been detected at all stages of the star formation process, from dark clouds (e.g., Walmsley et al. 1980) to protoplanetary disks (Chapillon et al. 2012) to comets (e.g., Bockelée-Morvan et al. 2000). While small cyanopolyynes such as HC_3N and HC_5N are regularly observed with (sub)millimeter telescopes, much less is known about the presence and evolution of heavy species (e.g., chains with more than seven carbon atoms) that have their peak of emission at longer wavelengths. Even the relatively simple and abundant cyanotriacetylene (HC_7N) has only been detected in a handful of solar-type prestellar cores and protostars (e.g., Cernicharo et al. 1986; Gupta et al. 2009; Cordiner et al. 2012; Friesen et al. 2013; Jaber Al-Edhari et al. 2017). However, large carbon chains might have a crucial role in the heritage of organic material from the pre- and protostellar phase to the objects of the newly formed planetary system, such as asteroids and comets (e.g., Mumma & Charnley 2011).

Despite the importance of large carbon species in the astrobiological context and its potential diagnostic power, only the starless core TMC-1 has been extensively explored so far (e.g., Cernicharo et al. 2021). This object has been the target of two deep surveys: the Green Bank Telescope (GBT) Observations of TMC-1: Hunting Aromatic Molecules (GOTHAM; McGuire et al. 2020) and the *Q*-band Ultrasensitive Inspection Journey to the Obscure TMC-1 Environment (QUIJOTE) projects, which extensively investigated the cyanopolyyne

chemistry in this source. In particular, they revealed for the first time several cyanopolyyne isotopologues and isomers (such as HC_4NC and HC_6NC; Cernicharo et al. 2020), as well as the presence of $HC_{11}N$ (Loomis et al. 2021), the largest cyanopolyyne so far discovered in the ISM. However, TMC-1 actually is a starless core that does not have any sign of collapsing and becoming eventually a planetary system. In this respect, the study of large cyanopolyynes in a prestellar core, which is believed to eventually form a solar-type planetary system, is particularly important.

L1544, in the Taurus molecular cloud complex at a distance of 170 pc (e.g., Galli et al. 2019), is considered the prototype of prestellar cores, being on the verge of gravitational collapse (e.g., Caselli & Ceccarelli 2012). Its central high density ($\sim 10^6$ cm^{-3}) and very low temperature ($\sim$7 K) result in the peculiar chemistry typical of cold and CO depleted gas, namely, a very high deuteration of species (e.g., Caselli et al. 1999; Ceccarelli et al. 2007; Crapsi et al. 2007; Caselli et al. 2022). In the external layers, however, different rich chemical processes take place that lead to the formation of interstellar complex organic molecules (iCOMs) and carbon chains (e.g., Bizzocchi et al. 2014; Jiménez-Serra et al. 2016; Vastel et al. 2016; Punanova et al. 2018; Ceccarelli et al. 2022). Indeed, recent (single-dish) IRAM 30 m observations in the millimeter window show the presence of small carbon chains such as HC_3N, c-C_3H_2, C_3H, C_4H, C_2O, and C_3O over extended portions of L1544 (Vastel et al. 2014; Spezzano et al. 2017; Urso et al. 2019).

We carried out a pilot line survey in the X (8.0–11.6 GHz) and Ku (13.5–14.4 GHz) bands with the GBT toward L1544. The goal of the project is to obtain the first census of molecular lines in this radio spectral range toward a well-known and established analog of the solar system precursor. In this first article, we report the study of the cyanopolyynes.

The article is organized as follows. We report the observations and the detected lines in Section 2. In Section 3, we analyze the detected cyanopolyyne lines to derive constraints on the physical conditions of the emitting gas. To this end, we carried out new computations to derive the collisional coefficients of HC_5N and HC_7N with H_2 in Section 4. Section 5 reports the implications of our new observation for the understanding of the cyanopolyyne chemistry in the earliest phases of a solar-type planetary system, and Section 6 concludes the article.

2. Observations and Results

2.1. Observations

The observations presented here were carried out between 2019 June and 2020 February on the GBT, under project codes AGBT19A_048 and AGBT20A_135. The target source L1544 was observed at the coordinates $\alpha_{J2000} = 05^h04^m16\overset{s}{.}60$, $\delta_{J2000} = +25°10'48\overset{''}{.}0$. The source calibrator 0530+1331 was used to perform pointing and focus. Observations were performed using position switching mode with an ON-OFF throw position of 1°. Two receivers were used to cover the X band (8.0–11.6 GHz) and the Ku band (13.5–14.4 GHz) in combination with the VEGA spectrometer in high-resolution mode. The bandwidth per spectral window was 187.5 MHz, with 131,072 channels corresponding to a resolution of 1.4 kHz (0.05 km s^{-1} at 9 GHz). The rms is typically $\sim$5 mK in a channel of $\sim$1.4 kHz. The telescope half-power beamwidth (HPBW) varies between $\sim 54''$ in Ku band and $1\overset{'}{.}4$ in X band, corresponding to $\sim$9180 au and $\sim$14,280 au at the source distance. The calibration was performed using GBTIDL. The spectra are first inspected by eye and cleaned of any artifacts. Successively, each scan is corrected for Doppler tracking and calibrated in flux using the internal noise diodes from the receiver. The calibrated scans for a single observing session are then noise-weighted averaged. The baseline subtraction is performed by automatically identifying the line-free channels and performing a polynomial fit. The spectra were finally corrected for the GBT telescope efficiencies.[13] Calibration uncertainties are estimated to be $\sim$20%.

2.2. Results

We detected several bright emission lines from cyanopolyynes in L1544. More specifically, we detected three emission lines from HC_3N, nine lines from HC_5N, five lines from HC_7N, and nine lines from HC_9N (see Table 1). The threshold for detection is a signal-to-noise ratio larger than 3σ at the line peak. Line identification has been performed using the Cologne Database for Molecular Spectroscopy[14] (Müller et al. 2001, 2005). Table 1 reports the list of the detected transitions with their spectroscopic and derived line parameters, namely the line frequency, ν, the upper-level energy, E_{up}, the line strength, $S\mu^2$, the line peak intensity in main-beam temperature scale, T_{peak}, the rms noise, rms, and the integrated intensity, I_{int}. The upper-level energy of the detected lines is low, $E_{up} \leqslant 10$ K. The line analysis has been performed using the GILDAS[15] CLASS package. The observed spectra are reported in Figures 1–4.

The observed cyanopolyyne lines show a double-peaked profile, revealed thanks to the very high spectral resolution ($\sim$1.4 kHz, corresponding to $\sim$30 m s^{-1} at 14 GHz) provided by the GBT. The two emission peaks are located at +7.1 and +7.3 km s^{-1}, with a dip located at the systemic source velocity (+7.2 km s^{-1}). The redshifted peak is brighter than the blueshifted one by a factor between 3 and 5, depending on the line. We report for the first time toward the source the heavier cyanopolyyne HC_9N, while HC_3N, HC_5N, and HC_7N have been previously observed in L1544 (Snell et al. 1981; Cernicharo et al. 1986; Quénard et al. 2017; Hily-Blant et al. 2018). The HC_3N spectra previously observed at the IRAM 30 m have a spectral resolution $\sim$0.2 km s^{-1}, and they do not reveal the double-peak profile. Interestingly, the velocities of the two peaks are consistent with the blue- and redshifted velocities revealed by the peak velocity distribution derived by Spezzano et al. (2016) in c-C_3H_2 using the IRAM 30 m. In addition, the spectral profiles of the present data set are well consistent with those at high spectral resolution (down to $\simeq$0.04 km s^{-1}) previously observed at GBT toward L1544 in other complex C-bearing species such as C_4H, C_6H, and C_6H^- (Gupta et al. 2009).

3. Physical Conditions and Abundance Ratios

3.1. Full Radiative Transfer Modeling

In order to interpret the line profiles, we use the full radiative transfer code LOC (Juvela 2020) with a 1D model that assumes spherically symmetric distribution of physical structures,

[13] https://www.gb.nrao.edu/scienceDocs/GBTpg.pdf
[14] https://cdms.astro.uni-koeln.de/
[15] http://www.iram.fr/IRAMFR/GILDAS

Table 1
List of Transitions and Line Properties (in T_{MB} Scale) of the Cyanopolyyne Emission

Transition	ν[a] (GHz)	E_{up} [a] (K)	$S\mu^2$ [a] (D^2)	T_{peak} (mK)	rms (mK)	I_{int} [b] (mK km s^{-1})
			HC_3N			
HC_3N 1–0, $F = 1$–1	9.0970	0.44	4.6	941	5	247 (1)
HC_3N 1–0, $F = 2$–1	9.0983	0.44	7.7	1485	5	397 (1)
HC_3N 1–0, $F = 0$–1	9.1003	0.44	1.5	333	5	90 (1)
			HC_5N			
HC_5N 3–2, $F = 2$–1	7.98778	0.77	33.8	121	8	30 (1)
HC_5N 3–2, $F = 3$–2	7.98799	0.77	50.0	229	8	47 (1)
HC_5N 3–2, $F = 4$–3	7.98804	0.77	72.3	317	9	67 (1)
HC_5N 3–2, $F = 2$–2	7.98992	0.77	6.2	43	6	7 (1)
HC_5N 4–3, $F = 4$–4	10.64923	1.28	4.7	54	6	9 (1)
HC_5N 4–3, $F = 3$–2	10.65056	1.28	53.6	567	6	108 (1)
HC_5N 4–3, $F = 4$–3	10.65065	1.28	70.3	700	7	141 (1)
HC_5N 4–3, $F = 5$–4	10.65068	1.28	91.7	896	6	179 (1)
HC_5N 4–3, $F = 3$–3	10.65249	1.28	4.7	61	6	13 (1)
			HC_7N			
HC_7N 8–7, $F = 7$–6	9.02399	1.95	161.1	92	5	20 (1)
HC_7N 8–7, $F = 8$–7	9.02401	1.95	183.0	109	5	46 (1)
HC_7N 8–7, $F = 9$–8	9.02402		207.7			
HC_7N 9–8, $F = 8$–7	10.15200	2.44	184.5	217	4	93 (1)
HC_7N 9–8, $F = 9$–8	10.15201		206.5			
HC_7N 9–8, $F = 10$–9	10.15202		231.1			
HC_7N 10–9, $F = 10$–10	11.28900	3.00	207.9	323	8	133 (2)
HC_7N 10–9, $F = 10$–9	11.28001		230.0			
HC_7N 10–9, $F = 11$–10	11.28001		254.4			
HC_7N 13–12, $F = 12$–11	14.66399	4.93	277.8	443	7	151 (1)
HC_7N 13–12, $F = 13$–12	14.66399		300.3			
HC_7N 13–12, $F = 14$–13	14.66400		324.4			
			HC_9N			
HC_9N 14–13, $F = 13$–12	8.13450	2.93	350.5	32	5	14 (1)
HC_9N 14–13, $F = 14$–13	8.13450		376.7			
HC_9N 14–13, $F = 15$–14	8.13451		404.6			
HC_9N 15–14, $F = 14$–13	8.71553	3.35	377.6	41	5	13 (1)
HC_9N 15–14, $F = 15$–14	8.71554		376.7			
HC_9N 15–14, $F = 16$–15	8.71554		431.7			
HC_9N 16–15, $F = 15$–14	9.29657	3.79	404.8	42	5	15 (1)
HC_9N 16–15, $F = 16$–15	9.29657		430.9			
HC_9N 16–15, $F = 17$–16	9.29657		458.9			
HC_9N 17–16, $F = 16$–15	9.87760	4.27	431.8	57	5	19 (1)
HC_9N 17–16, $F = 17$–16	9.87761		458.1			
HC_9N 17–16, $F = 18$–17	9.87761		486.0			
HC_9N 18–17, $F = 17$–16	10.45864	4.77	458.9	55	5	18 (1)
HC_9N 18–17, $F = 18$–17	10.45864		485.2			
HC_9N 18–17, $F = 19$–18	10.45864		513.0			
HC_9N 19–18, $F = 18$–17	11.03967	5.30	486.0	95	7	22 (1)
HC_9N 19–18, $F = 19$–18	11.03967		512.3			
HC_9N 19–18, $F = 20$–19	11.03967		540.1			
HC_9N 24–23	13.94483	8.37	1947.0	152	6	24 (1)
HC_9N 25–24	14.52586	9.06	2028.1	157	6	25 (1)
HC_9N 26–25	15.10689	9.79	2108.9	166	7	26 (1)

Notes. The columns report the transition and their frequency (GHz), the upper-level energy E_{up} (K), the line strength $S\mu^2$ (D^2), the line peak temperature (mK), the rms (mK), and the velocity-integrated line intensity I_{int} (mK km s^{-1}).
[a] Frequencies and spectroscopic parameters have been provided by de Zafra (1971) for HC_3N, Giesen et al. (2020) for HC_5N and HC_9N, and McCarthy et al. (2000) for HC_9N and retrieved from the Cologne Database for Molecular Spectroscopy (Müller et al. 2005).
[b] Errors on the integrated intensity do not include 20% of calibration.

characterized by volume density, $\rho(r)$, kinetic temperature, $T(r)$, and velocity field, including both microturbulence, σ_{turb}, and radial velocity, $V(r)$. We adopted the parameterized forms of $\rho(r)$, $T(r)$, and $V(r)$ following Keto & Caselli (2010) for L1544. The core radius is assumed to be 0.3 pc. In the modeling, linear discretization is used for the grids with a

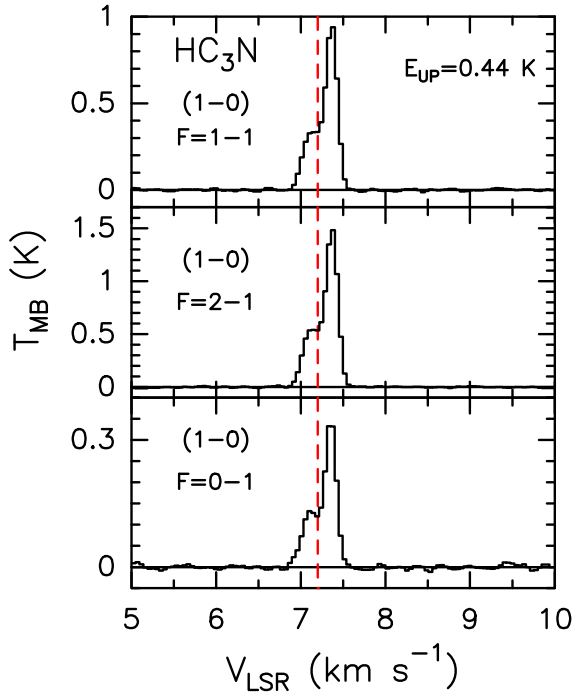

Figure 1. HC_3N transitions observed toward L1544 with the GBT. The vertical dashed lines mark the ambient LSR velocity (+7.2 km s^{-1}; Tafalla et al. 1998). The upper-level energy of each transition is reported on the right inside the top panel.

physical resolution of 60 au. We then convolved the output spectral cube with the corresponding observational beam for each frequency. We tested several abundance profiles for HC_3N, with both constant abundance profile and constant abundance profile with depletion in the inner few thousand au of the core. While we are able to reproduce the overall intensity of the lines with abundances of a few $\times 10^{-9}$, we cannot reproduce the observed line profiles. Figure 5 shows the results of one of our tests, run using a constant abundance profile of 5×10^{-9} with respect to H_2 and complete freeze-out toward the inner 5000 au of the core. The 1–0 transition of HC_3N, given the very low critical density ($\sim 10^3$ cm^{-3}), traces the outer layers of the core, as also found by, e.g., Liu et al. (2022) in cold Planck clumps, and it is likely that the line profile that we observe is showing us the asymmetry in these outer layers. As a consequence, by using a spherical model we cannot reproduce the line profiles. The profiles of many emission lines have been successfully reproduced with the Keto & Caselli physical structure of L1544 using transitions with larger critical densities (10^4–10^5 cm^{-3}) with respect to the 1–0 transition of HC_3N. Likely the spherical symmetry approximation is not realistic for transitions tracing low-density gas.

3.2. Large Velocity Gradient Modeling

In order to understand the nature and the spatial origin of the gas emitting in cyanopolyynes, we analyzed the observed HC_5N, HC_7N, and HC_9N lines via a non-LTE large velocity gradient (LVG) approach. To this end, we used the code GRELVG, initially developed by Ceccarelli et al. (2003). We used the collisional coefficients of HC_5N, HC_7N, and HC_9N with para-H_2 between 10 and 100 K, computed from the HC_3N collisional coefficients as described in Section 4. The first 50 levels of each species are included, which means transitions with upper-level energies of 160, 70, and 35 K for HC_5N, HC_7N, and HC_9N, respectively. We will discuss the impact of these limits when analyzing the results of the modeling. To compute the line escape probability as a function of the line optical depth, we adopted a semi-infinite expanding slab geometry (Scoville & Solomon 1974) and a line width equal to 0.4 km s^{-1}, following the observations.

We ran several grids of models to sample the χ^2 surface in the parameter space. Specifically, we varied the HC_5N column density $N(HC_5N)$ from 1×10^{12} cm^{-2} to 2×10^{15} cm^{-2}, the HC_5N/HC_7N abundance ratio f_{5-7} from 3 to 9, the HC_5N/HC_9N abundance ratio f_{5-9} from 9 to 49, the H_2 density n_{H2} from 100 to 10^6 cm^{-3}, and the temperature T_{gas} from 5 to 100 K. We then fitted the measured HC_5N, HC_7N, and HC_9N velocity-integrated line intensities by comparing them with those predicted by the model, leaving $N(HC_5N)$, f_{5-7}, f_{5-9}, n_{H2}, T_{gas}, and the emitting size θ as free parameters.

We proceeded in two steps. In a first step, we considered the three species independently and obtained constraints on their column densities and the emitting gas properties (θ, n_{H2}, T_{gas}). In a second step, we fitted the lines from the three species simultaneously, obtaining constraints on all parameters: $N(HC_5N)$, f_{5-7}, f_{5-9}, θ, n_{H2}, and T_{gas}.

3.2.1. Step 1: HC_5N, HC_7N, and HC_9N Separate Fit

HC_5N: Given the limited number (two) of lines and range of upper-level energy, only a lower limit to the $N(HC_5N)$ is obtained, $\geqslant 4 \times 10^{13}$ cm^{-2}, with an emitting size of about 100″.

HC_7N: With four lines, the HC_7N fitting constrains better the gas parameter than the HC_5N one. The column density $N(HC_7N)$ is constrained at 1σ in the range $(0.6-3) \times 10^{13}$ cm^{-2}, where the emitting sizes are from 100″ to 38″, respectively. Both the gas temperature and densities are difficult to constrain, as they depend on the HC_7N column density (see Section 3.2.2 below).

HC_9N: The column density $N(HC_9N)$ is, at 1σ, in the range $(0.1-3) \times 10^{13}$ cm^{-2}, where the emitting sizes are from 150″ to 38″, respectively. Again, the gas temperature and densities are difficult to constrain, as they depend on the HC_9N column density (see Section 3.2.2 below).

3.2.2. Step 2: HC_5N, HC_7N, and HC_9N Simultaneous Fit

We assumed that the three cyanopolyynes originate in the same gas. This assumption is based on the similarity of the line shapes of the three species. We considered all the lines detected in the observations presented here, namely a total of 18 lines, which leads to 12 degrees of freedom in the fit.

We started by exploring the χ^2 surface over large ranges and gradually zoomed in to smaller ones to be sure not to miss local minima. In practice, each grid consisted of about 10^4 models, and we ran a dozen grids. The results of the analysis are shown in Figure 6 and reported in Table 2.

First, the top panel of Figure 6 shows the reduced χ^2 as a function of the HC_5N/HC_7N and HC_5N/HC_9N abundance ratios. The best fit (reduced $\chi^2 = 0.31$) is obtained for $f_{5-7} = 6^{+1}_{-2}$ and $f_{5-9} = 25 \pm 10$, along a banana-like curve with $HC_7N/HC_9N = 4 \pm 1$. The best fit is obtained at $HC_5N/HC_7N = 6$ and $HC_7N/HC_9N = 4$. With these values, the HC_5N column density $N(HC_5N)$ is equal to $\sim(3–20) \times 10^{13}$ cm^{-2} and θ is $\sim$100″–32″ (the larger $N(HC_5N)$, the smaller θ), as shown in Figure 6. The lowest χ^2 is obtained for $N(HC_5N) = 4.3 \times 10^{13}$ cm^{-2} and $\theta = 80''$. With these values,

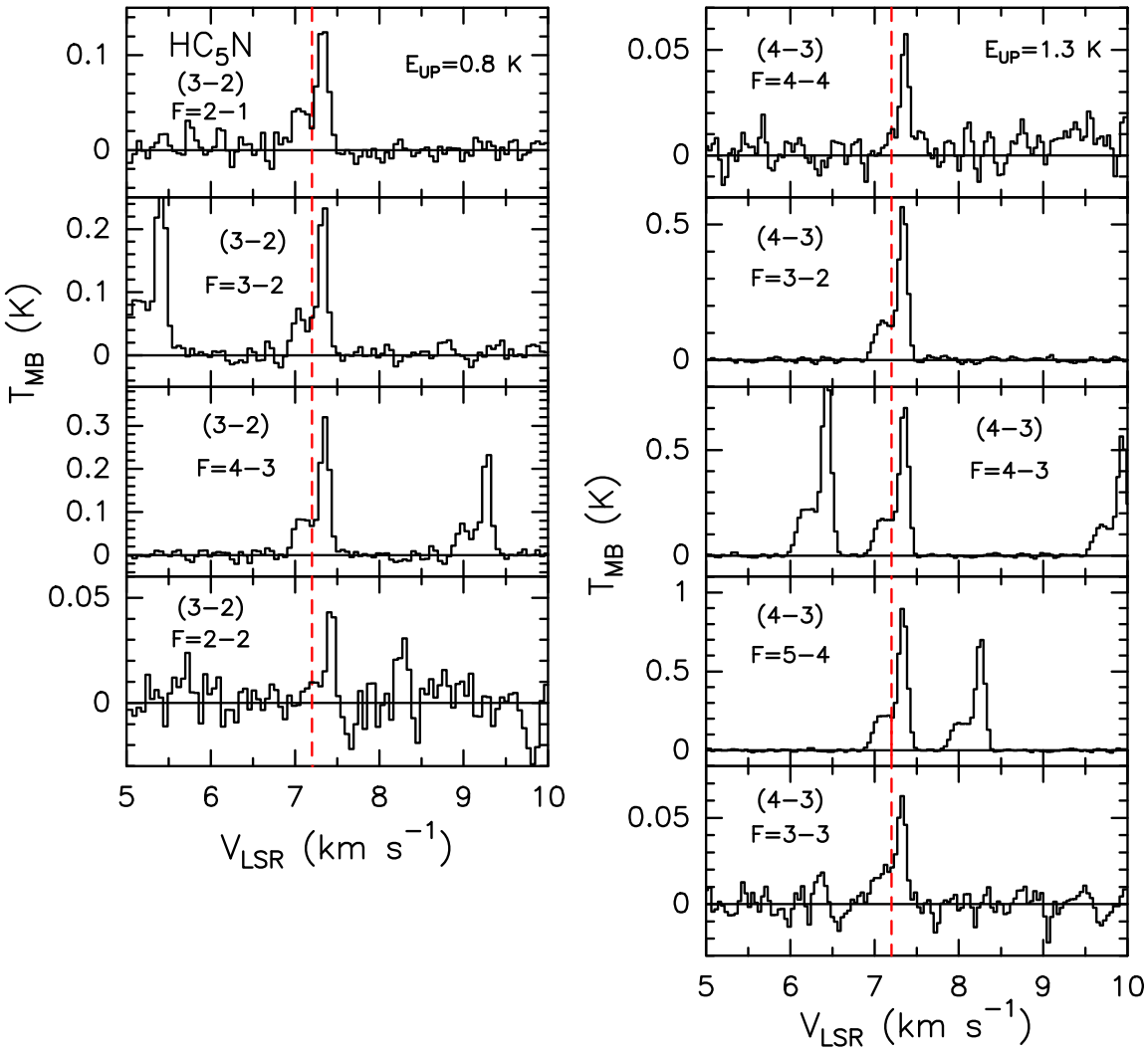

Figure 2. HC_5N transitions observed toward L1544 with the GBT. The vertical dashed lines mark the ambient LSR velocity (+ 7.2 km s^{-1}; Tafalla et al. 1998). The upper-level energy of each transition is reported on the right inside the top panels.

the lowest χ^2 is obtained for $T_{gas} = 7.5$ K and $n_{H2} = 100$ cm^{-3}. At the 1σ level the temperature is between 5 and 12 K and the density remains unconstrained (Figure 6). The observed and predicted intensities of all the lines are shown in the bottom panel of Figure 6. The HC_5N, HC_7N, and HC_9N lines are all optically thin (the highest τ is 0.6 for the HC_5N $J = 4$ line), and the lines are moderately subthermally populated ($T_{ex} \sim$ 6–7 K).

3.2.3. Impact of the Limited Number of Considered Levels

Finally, we comment on the possible impact on the gas temperature caused by the limited number of levels, only 50 for the three cyanopolyynes. While the number of levels of HC_5N is enough for a reasonable analysis for temperatures below 30 K, the limited number of levels of HC_7N and HC_9N may, in principle, be problematic. However, since the gas temperature derived from the previous LVG analysis is lower than 12 K, the analysis is probably not greatly impacted by the range of energy levels probed by the observations. For example, the excitation temperatures T_{ex} of the HC_7N $J = 13$–12 and HC_9N $J = 26$–25 lines are 7.3 and 6.95 K, respectively, when the gas kinetic temperature is 7.5 K. Therefore, the highest levels of HC_7N and HC_9N are probably not populated, which makes the above analysis reliable.

4. Collisional Coefficients

To the best of our knowledge, no collisional data are available for the HC_5N and HC_7N molecules. However, as already suggested by Snell et al. (1981), HC_5N–H_2 and HC_7N–H_2 rate coefficients may be estimated from HCN–H_2 and HC_3N–H_2 rate coefficients considering that the rate coefficients will be proportional to the size of the molecules.

We considered the HC_3N–H_2 rate coefficients as a reference for the estimation of HC_5N–H_2 and HC_7N–H_2 rate coefficients. As a crude approximation, HC_5N and HC_7N are, respectively, 1.5 and 2 times longer than HC_3N, whereas HCN is 2 times shorter than HC_3N.

Snell et al. (1981) scale the HC_3N rate coefficients by a factor 1.5 and 2 to get HC_5N and HC_7N rate coefficients, respectively. They also checked that HCN and HC_3N rate coefficients obey the same rules. However, as noticed by Snell et al. (1981), the scaling factors are averages, and significant deviations occur depending on the transition and the temperature considered.

In this work, in order to improve the accuracy of the estimation, we consider scaling factors depending on the size of the molecule (1.5 for HC_5N and 2 for HC_7N) but also on the transition and the temperature considered. Indeed, the ratio of HC_3N–H_2 over HCN–H_2 rate coefficients was also used to

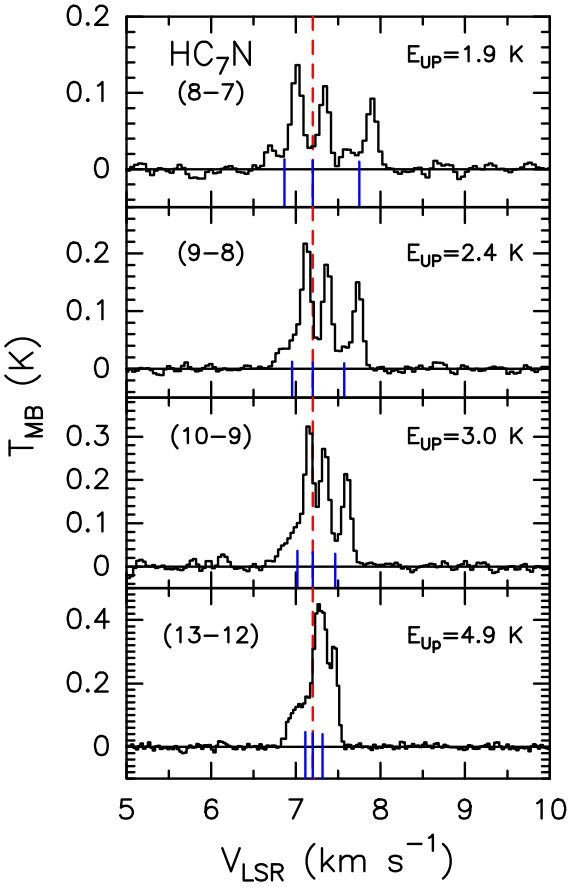

Figure 3. HC_7N transitions observed toward L1544 with the GBT. The vertical dashed lines mark the ambient LSR velocity (+7.2 km s^{-1}; Tafalla et al. 1998). The upper-level energy of each transition is reported on the right inside each panel.

evaluate the HC_5N–H_2 and HC_7N–H_2 as follows:

$$k_{J\to J'}^{\mathrm{HC_7N-H_2}}(T) = k_{J\to J'}^{\mathrm{HC_3N-H_2}}(T)\frac{k_{J\to J'}^{\mathrm{HC_3N-H_2}}(T)}{k_{J\to J'}^{\mathrm{HCN-H_2}}(T)} \quad (1)$$

and

$$k_{J\to J'}^{\mathrm{HC_5N-H_2}}(T) = \frac{1}{2}(k_{J\to J'}^{\mathrm{HC_3N-H_2}}(T) + k_{J\to J'}^{\mathrm{HC_7N-H_2}}(T)). \quad (2)$$

The HCN–H_2 rate coefficients of Ben Abdallah et al. (2012) and the HC_3N–H_2 rate coefficients of Wernli et al. (2007) were used in the above formula.

Using such an approach, we expect to have a better description of large ΔJ ($J' - J \gg 1$) for collisionally induced transitions and for very low temperatures. In the astrophysical models, the HC_9N–H_2 rate coefficients were considered to be the same as the HC_7N–H_2 ones. It should be noted that the accuracy of the present calculations is expected to be accurate only to within about an order of magnitude. Future calculations of rate coefficients for HC_5N and HC_7N molecules have to be performed using a more reliable approach.

5. Discussion

5.1. Origin of the Cyanopolyyne Emission in L1544

The high spectral resolution provided by the present observations allows us to resolve in detail the shape of the observed cyanopolyyne lines (see Section 2.2). Specifically, the lines present a double peak with the redshifted intensity brighter than the blueshifted one (Section 2.2). Previous maps by Spezzano et al. (2016) and Spezzano et al. (2017) show that the emission of carbon chains is concentrated in the southeast region of L1544, in contrast with that of methanol, whose lines are bright in the north. The velocity in the two regions is slightly different, with the C-chain peak redshifted with respect to the velocity of the methanol peak. In the present observations, the velocity of the cyanopolyyne redshifted peak is consistent with that of the carbon chain emitting region. Therefore, the fact that the cyanopolyyne lines are brighter in the redshifted peak implies that they mainly originate in the southeast region of the L1544 core. These results support the idea that the carbon chain abundance is enhanced toward the external part of the core, where material is more exposed to the interstellar field radiation. The southern part of the source is particularly exposed since it is located at the edge of the cloud (André et al. 2010), and this would increase the free carbon atoms available to form long chains (see also Spezzano et al. 2016). The line profiles observed with the GBT are consistent with those observed by Gupta et al. (2009) in other carbon chains but clearly different from those observed in high-density gas tracers toward L1544 (e.g., N_2D^+ and N_2D^+; Caselli et al. 2002, 2017), supporting this interpretation.

The non-LTE LVG analysis (Section 3.2) indicates that the cyanopolyyne emission originates predominantly from an extended region (∼13,600 au in radius) at low temperature (5–12 K). Unfortunately, the gas density is unconstrained other than being larger than ∼100 cm^{-3}.

The derived temperature is in agreement with the dust temperature measured with Herschel and shown in Figure 7. SPIRE is only sensitive to the extended emission, and the core regions probed by the GBT have a dust temperature ranging between 11.5 and 15 K. On the other hand, other molecular tracers, such as NH_3 and its isotopologues, show that the gas temperature decreases toward the central part of the core down to ∼7 K (Crapsi et al. 2007).

However, the analysis has several limitations, which should be taken into account. First, the physical model of the source used in our analysis of Section 3.1, i.e., the one by Keto & Caselli (2010), assumes spherical symmetry, within the observed region. On the contrary, the non-LTE LVG analysis in Section 3.2 assumes a semi-infinite slab. On the other hand, the spectral profiles suggest that the cyanopolyyne emission is nonhomogeneously distributed and the modeling does not distinguish the different emitting components. The results of the modeling would then be representative of the physical conditions of the main emitting component, but they could be locally different. Another assumption of the non-LTE LVG modeling in Section 3.2 is that all the cyanopolyynes are cospatial and trace the same gas. Although this hypothesis is supported by the similar line profiles, it cannot be verified only using single-dish GBT observations. Finally, recent observations have shown the presence of deuterated carbon chains (c-C_3HD and c-C_3D_2) toward the dusty peak at the center of the core (Giers et al. 2022). This would suggest that even if the bulk of the emission comes from the external layers, a significant fraction of molecular species rich in carbon can still be present in the densest regions of the core, where free carbon atoms are produced by the CO destruction from the molecular ions created by cosmic rays (such as He^+), as first proposed by Ruffle et al. (1999). Further interferometric

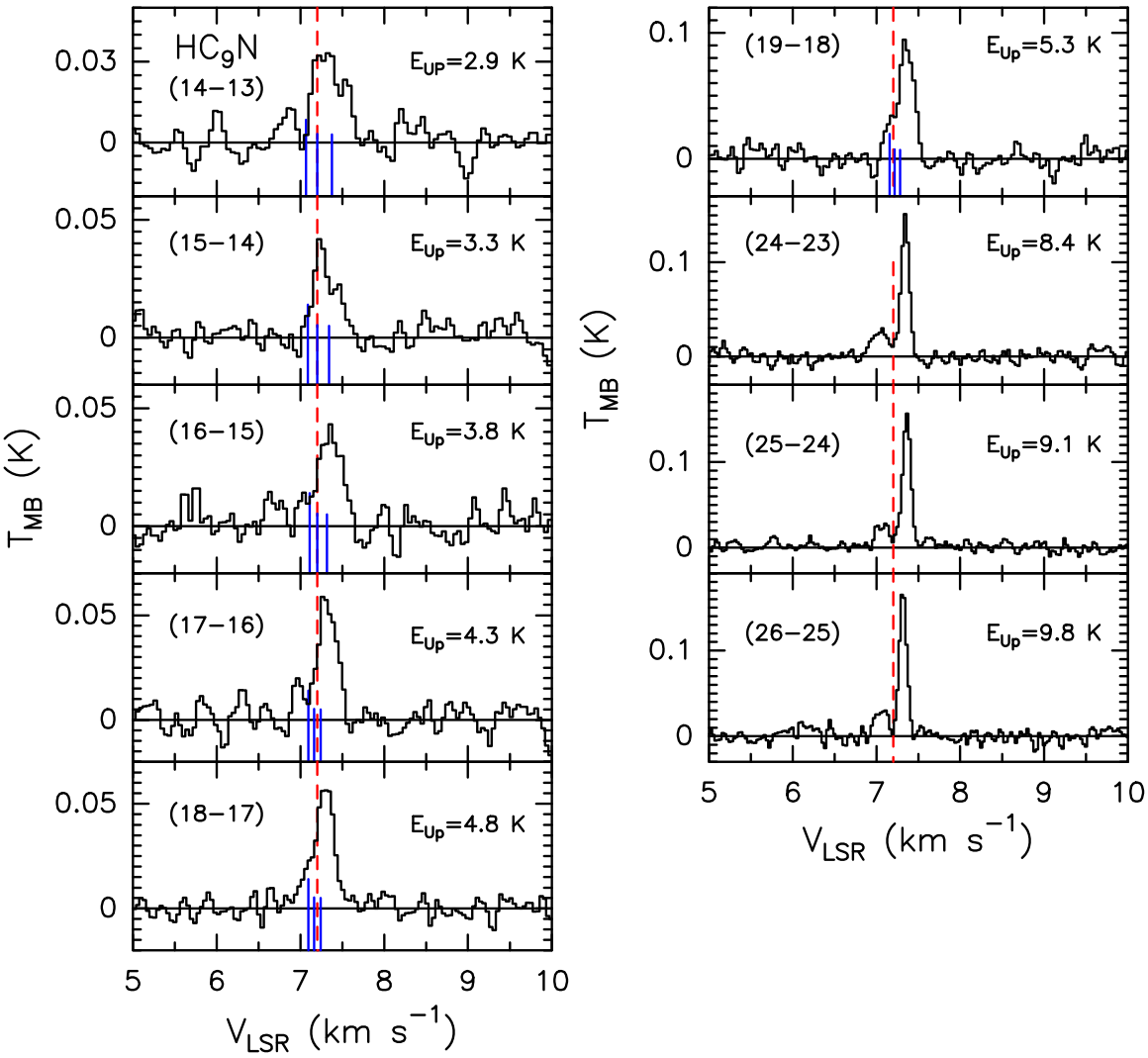

Figure 4. HC_9N transitions observed toward L1544 with the GBT. The vertical dashed lines mark the ambient LSR velocity (+7.2 km s^{-1}; Tafalla et al. 1998). The upper-level energy of each transition is reported on the right inside each panel. The blue lines indicate the position of the hyperfine components.

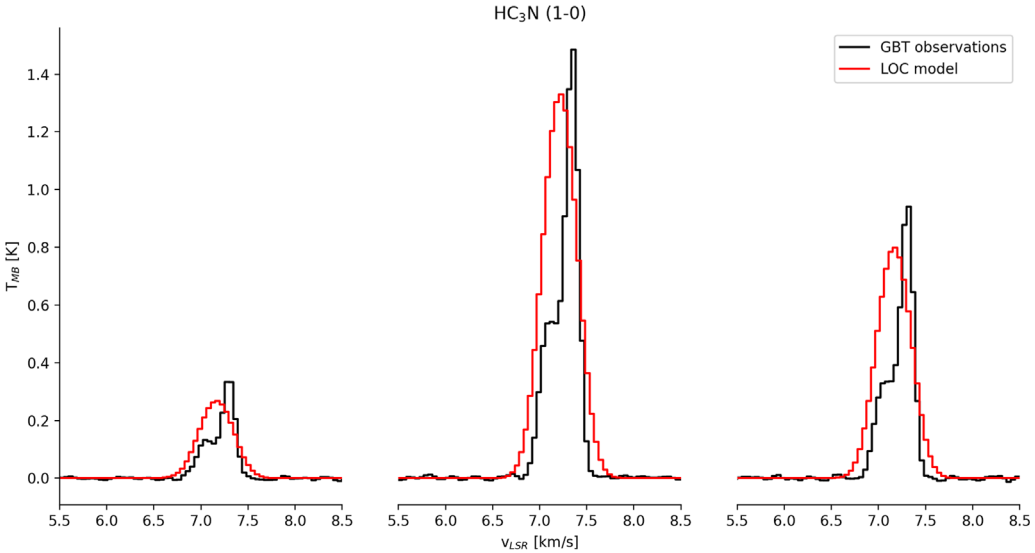

Figure 5. Comparison between the observed HC_3N line profiles and the theoretical profiles predicted using the radiative transfer code LOC (see Section 3.1). The model, assuming spherical symmetry distribution, reproduces the line intensities but not the shape of the profiles. This suggests an asymmetric distribution of cyanopolyynes across the core, with the redshifted component brighter than the blueshifted one.

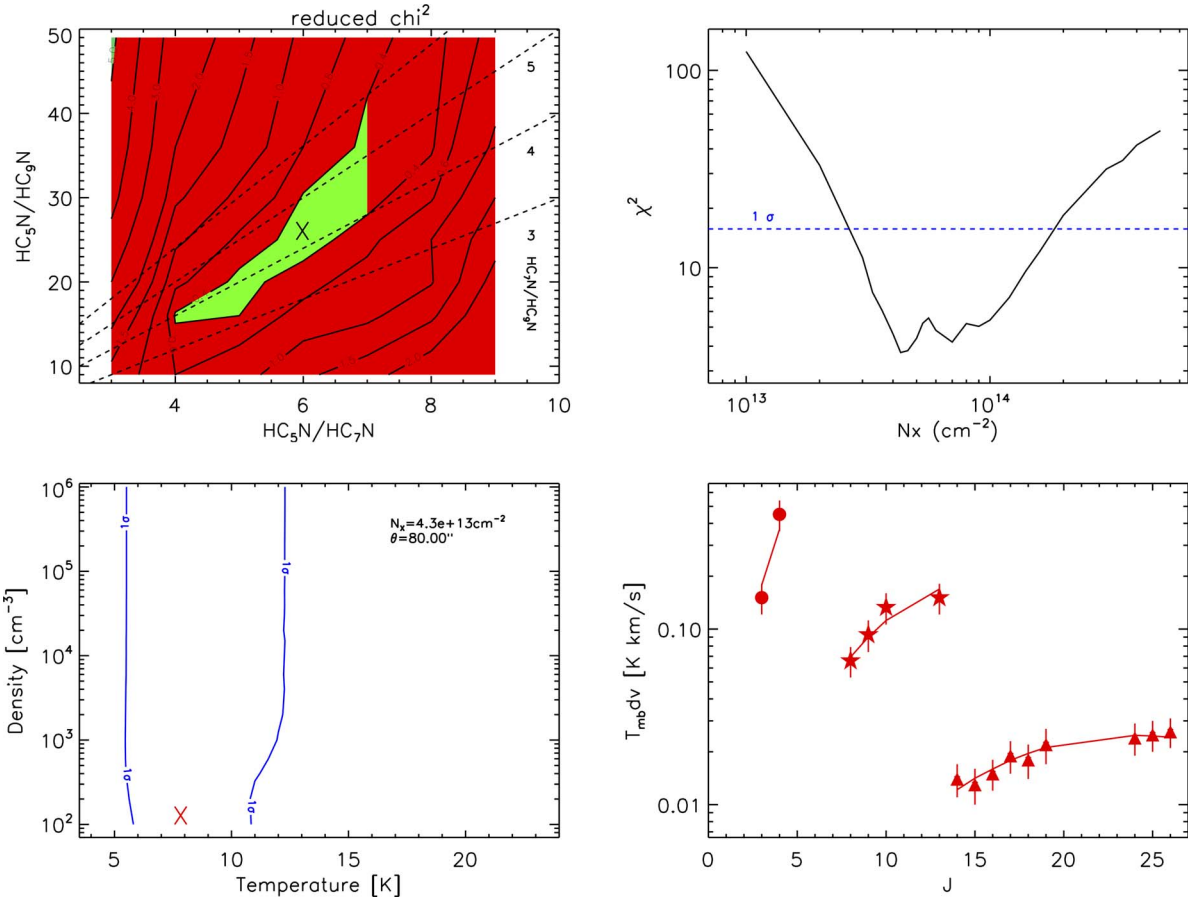

Figure 6. Results from the χ^2 minimization obtained fitting simultaneously the HC_5N, HC_7N, and HC_9N velocity-integrated line intensities. Top left panel: reduced χ^2 as a function of the HC_5N/HC_7N and HC_5N/HC_9N abundance ratios. The cross shows the best fit, and the green area shows the 1σ uncertainty parameter space. The dashed lines show the HC_7N/HC_9N ratio. Top right panel: minimum χ^2 obtained at each HC_5N column density $N(HC_5N)$ (minimized with respect to the gas temperature and density) as a function of $N(HC_5N)$. The dashed horizontal line shows the 1σ interval. Bottom left panel: contour plot of the χ^2 as a function of the density and temperature, obtained for the best-fit HC_5N column density of 4.3×10^{13} cm^{-2} and source size of $80''$ (see top left panel). The red cross indicates the best-fit gas density and temperature, and the blue curve indicates the 1σ interval. Bottom right panel: observed velocity-integrated line intensities of HC_5N (circles), HC_7N (stars), and HC_9N (triangles) and the modeled ones (red curves) as a function of the upper J of the transitions, computed at the best fit (see text).

Table 2
Results of the Non-LTE LVG Analysis

Parameter (Units)	Best Fit	1σ Range
θ (arcsec)	80	32–100
$N(HC_5N)$ ($\times 10^{13}$ cm^{-2})	4.3	3–20
$N(HC_5N)/N(HC_7N)$	6	4–7
$N(HC_7N)/N(HC_9N)$	4	3–5
H_2 density (cm^{-3})	100	$\geqslant$100
Gas temperature (K)	7.5	5–12

Note. Best-fit emitting region size (row 1), HC_5N column density (row 2), HC_5N/HC_7N and HC_5N/HC_9N column density ratios (rows 3 and 4, respectively), H_2 density (row 5), and gas temperature (row 6). For each parameter the 1σ range is reported in the second column.

observations are needed to map the cyanopolyyne distribution across the core. In this respect, the next generation of radio interferometers such as SKA[16] and ngVLA[17] will be a major step forward.

[16] https://www.skao.int/
[17] https://ngvla.nrao.edu/

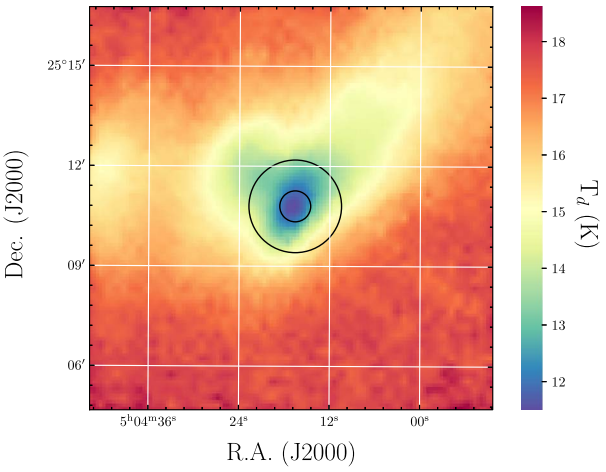

Figure 7. Dust temperature calculated from l/SPIRE data at 250, 350, and 500 μm observations toward L1544 and presented in Spezzano et al. (2016). We show superposed in black the GBT HPBWs in the two observed bands.

5.2. Comparison of L1544 with Other Sources

Cyanopolyyne emission is ubiquitous in the ISM. The simplest cyanopolyyne, HC_3N, was one of the first molecular

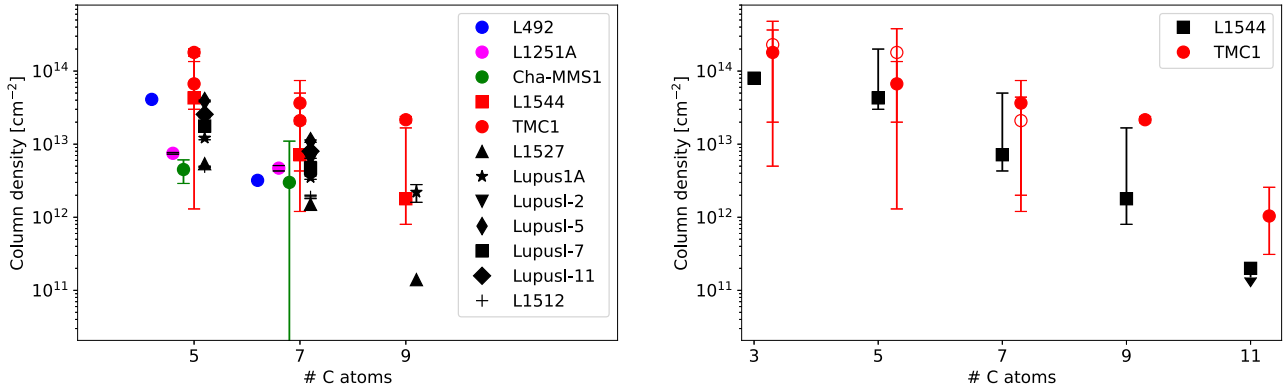

Figure 8. Comparison between the cyanopolyyne column densities measured in different star-forming regions. Left panel: comparison of column densities of HC_5N, HC_7N, and HC_9N. We indicate with the same color the cold cores located in the same star-forming regions. The cyanopolyyne emission is commonly detected in several star-forming regions, and the column densities are in agreement within one order of magnitude, considering the errors and the different instruments. The measurements are taken from the references in Table 3. Right panel: comparison between the cyanopolyyne abundances from HC_3N to $HC_{11}N$ measured in TMC-1 and L1544 (this work). For TMC-1, the filled circles are from Loomis et al. (2021), while the open circles refer to Cernicharo et al. (2020) and Cabezas et al. (2022).

Table 3
Cyanopolyyne Abundances in Starless Cores

Star-forming Region	Source	T_{ex} (K)	$N(HC_5N)$ (10^{12} cm^{-2})	$N(HC_7N)$ (10^{12} cm^{-2})	$N(HC_9N)$ (10^{12} cm^{-2})	References
Taurus	TMC-1	8	66.9 (1.3)	36.5 (1.3)	22 (2)	1
Taurus	TMC-1	8.6 (0.2)–7.6 (0.2)	180 (20)	21 (2)	⋯	2, 3
Taurus	L1527 IRAS 04368+2557	12.3	5.4	1.5	0.14	4
Lupus	Lupus-1A	10.0 (0.2)	12.1 (0.6)	3.5 (0.2)	2.2 (0.6)	5, 6, 7
Serpens	Serpens South 1a	7	12 (1)	6.0 (0.2)	3.1 (0.2)	8
Lupus	LupusI-2	11.5 (0.2)	22 (1)	6.1 (0.3)	⋯	7
Lupus	LupusI-5	11.2 (0.1)	39 (1)	11.0 (0.4)	⋯	7
Lupus	LupusI-7/8/9	10.2 (0.1)	17.7 (0.6)	4.7 (0.2)	⋯	7
Lupus	LupusI-11	11.9 (0.8)	25.6 (0.8)	8.0 (0.3)	⋯	7
Chameleon	Cha-MMS1	7 (1)	4.5 (1.6)	3 (8)	⋯	9
Taurus-Auriga	L1512	8.7 (0.7)	4.9 (0.1)	1.9 (0.1)	⋯	10
Cepheus	L1251A	6.2 (0.3)	7.5 (0.2)	4.7 (0.4)	⋯	10
Aquila Rift	L492	6.5–10	41	3.2	⋯	11

Note. (1) Loomis et al. 2021; (2) Cernicharo et al. 2020; (3) Cabezas et al. 2022; (4) Sakai et al. 2008; (5) Sakai et al. 2009; (6) Sakai et al. 2010; (7) Wu et al. 2019; (8) Li et al. 2016; (9) Cordiner et al. 2012; (10) Cordiner et al. 2011; (11) Hirota & Yamamoto 2006.

species detected outside of our Galaxy (Mauersberger et al. 1990). Small cyanopolyynes, up to HC_7N, have been detected in several starless and protostellar cores in different star-forming regions. However, few measurements exist so far of more complex cyanopolyynes such as HC_9N and $HC_{11}N$. Figure 8 (left panel) and Table 3 report the column densities measured in starless cores for cyanopolyynes from HC_5N to HC_9N. The only source for which all the cyanopolyynes from HC_3N to $HC_{11}N$ have been measured so far is TMC-1. Figure 8 (right panel) shows the comparison between L1544 (this work) and TMC-1 for cyanopolyynes from HC_3N to $HC_{11}N$. The deep surveys QUIJOTE and GOTHAM, performed on the source with the Yebes 40 m telescope and the GBT, respectively, lead to precise column density measurements. The major uncertainties are introduced by the assumption on the source size, which is highly covariant with the column density. Moreover, since the cyanopolyynes are very abundant in the source, the column densities of some species such as HC_5N and HC_9N could be affected by line opacity effects (Cernicharo et al. 2020, and private communication). For all these reasons, every comparison between the column densities measured in different sources has to be taken with caution. In TMC-1 all the cyanopolyynes have higher column densities than in L1544. In particular, $N(HC_3N)$ is higher by a factor 2–3, while $N(HC_5N)$ is higher by a factor 2–4, $N(HC_7N)$ by a factor 3–5, and $N(HC_9N)$ by a factor 12. The associated errors are quite large, and further constraints on the cyanopolyyne spatial distribution are needed in order to derive reliable abundance measurements and to effectively constrain the formation routes. However, the measurements in L1544 confirm that TMC-1 is not a unique source, but an active carbon chain chemistry is efficient also in other sources. The comparison between the HC_5N, HC_7N, and HC_9N column densities, reported in Figure 8 (left panel), suggests that the same chemistry could be active also in other cold cores. The fact that the measured column densities are similar within one order of magnitude, considering the different instruments and the large errors, may suggest that the heavy (with more than five carbons) cyanopolyyne formation is similar in different star-forming regions, once free gaseous carbon is available (see Section 5.4).

5.3. Chemistry of Cyanopolyynes

There is an ample consensus that the formation of cyanopolyynes is dominated by gas-phase reactions, in contrast with other large (e.g., with more than five atoms) species where

a dust grain surface chemistry can be at work (e.g., Ceccarelli et al. 2022). The reason is that unsaturated carbon chains, such as the cyanopolyynes, would rapidly be hydrogenated on the dust grain surfaces, so that, in order to produce the large amount of observed cyanopolyynes and to have them in the gas phase at the low temperatures where they are observed, the grain surface chemistry does not seem to be a viable solution.

Several gas-phase formation routes have been invoked in the literature. In general, for cyanopolyynes with more than five carbon atoms the following reactions are believed to be (the most) important (for a review see, e.g., Fukuzawa et al. 1998):

1. $C_{2n+2}H\,N \rightarrow HC_{2n+1}N + C$
2. $C_{2n}\,H_2 + CN \rightarrow HC_{2n+1}N + H$
3. $H_3C_{2n+1}N^+ + e^+ \rightarrow HC_{2n+1}N + H_2$
4. $H_2C_{2n+1}N^+ + e^+ \rightarrow HC_{2n+1}N + H,$

where $n \geqslant 2$.

Destruction routes are dominated by reactions with ions such as C^+, H^+, H_3^+, and HCO^+.

Loison et al. (2014) published a critical and general review of the reactions involving carbon chains, including cyanopolyynes up to HC_9N. They only list reactions (1), where they roughly evaluate the rate and branching ratios based on the capture theory and exothermicity of the products, respectively. Since the rate constants of reactions (3) are considered the same for HC_7N and HC_9N, and the destruction also occurs at the same rate, the ratios HC_5N:HC_7N:HC_9N would reflect the parent species ratios, namely HC_6:HC_8:HC_{10}. In other words, the $HC_nN/HC_{n+2}N$ ratios are inherited from the HC_n/HC_{n+2} one, as no reaction directly links HC_nN to $HC_{n+2}N$ in the Loison et al. (2014) scheme. Anyway, Loison et al. (2014) modeled the TMC-1 case and predicted the HC_5N:HC_7N:HC_9N ratios to be 1:0.14–0.3:0.10–0.13 at around 1×10^5 yr, where the model predictions agree better with observations (of several carbon chains). The two low and high values of each ratio are obtained assuming an elemental C/O abundance equal to 0.7 and 0.95, respectively. In general, the HC_7N:HC_9N ratio observed toward TMC-1 is larger than the predicted one, even though the error bars are relatively large. Likewise, the HC_5N:HC_7N:HC_9N ratios that we measured in L1544, about 1:6:4 (see Figure 6), are not consistent with the Loison et al. (2014) model predictions.

Reactions (2) were first mentioned and theoretically studied, via ab initio calculations, by Fukuzawa et al. (1998) for $n = 1$–4. These authors found that the reactions (2) with $n \geqslant 2$ are exothermic and the transition state barriers are all embedded. However, to the best of our knowledge, Fukuzawa et al. (1998) did not obtain the kinetics of the reactions. Reactions (3) and (4) were first introduced by Herbst & Leung (1989) and successively studied by Loomis et al. (2016). These authors obtained rough estimates of their rate constants by educated guess (extrapolation from similar reactions with small carbon chains or via the Langevin rate). However, again to the best of our knowledge, no specific experimental or theoretical ab initio studies exist in the literature on the rate constants and branching ratios of reactions (3) and (4). That said, Loomis et al. (2016) developed an astrochemical model to reproduce the observations of TMC-1 and predicted HC_5N:HC_7N:HC_9N ratios equal to about 1:4:4, which is in relatively good agreement with our measured ratios toward L1544. Finally, comparing observations of the $^{12}C/^{13}C$ cyanopolyynes toward TMC-1 and model predictions, Burkhardt et al. (2018) found that reactions (4) best reproduce the observations. Other processes could account for the formation of HC_7N and HC_9N. For instance, the reaction $C_3N + C_2H_2$ was proved to be very fast in CRESU experiments also at very low temperature (Fournier 2014). Therefore, the reactions of the C_3N radical with C_4H_2 and C_6H_2 are expected to be at least as fast because of the increased dimension of the molecular partner. In addition, reactions of C_4H (detected in this object) with HC_3N or HC_5N are also expected to be very fast, as the reaction of C_4H with acetylene is in the gas kinetics limit at very low T (Berteloite et al. 2010).

5.4. Age or UV Illumination?

As already mentioned above, the crucial point of the cyanopolyyne chemistry is the presence of gaseous carbon atoms, which, under standard conditions, are predominantly locked in CO molecules. Two general cases are possible: (1) either the object is very young and the locking of carbon atoms into CO is not complete yet, or (2) carbon atoms are liberated from CO thanks to processes such as intense UV illumination or cosmic-ray irradiation, able to destroy a fraction of CO. The first case has been advocated for TMC-1 (e.g., Agúndez & Wakelam 2013). Following the discussion of Section 5.1, the second case, specifically the intense UV illumination, seems to apply to L1544 (e.g., Spezzano et al. 2016, 2017).

In the case of UV illumination, the column density of the region where carbon is atomic is dictated by the penetration of the UV field, which is approximately given by a dust column density with a visual extinction of about 2–3 mag (e.g., Hollenbach & Tielens 1997; Snow & McCall 2006), which corresponds to $N(H_2) \sim (4\text{–}6) \times 10^{21}$ cm^{-2}. For example, the abundance of HC_7N (with respect to H_2) in L1544 would be $\sim 2 \times 10^{-9}$, where we used $N(HC_7N) \sim 8 \times 10^{12}$ cm^{-2} (Section 3.2).

In the case of a very young cloud, the column density of cyanopolyynes is, instead, determined by the H_2 column density of the cloud itself. For the TMC-1 cloud, the latest estimates indicate $N(H_2) \sim 1.5 \times 10^{22}$ cm^{-2}, which corresponds to a visual extinction of about 15 mag (Fuente et al. 2019). Assuming $N(HC_7N) \sim 2 \times 10^{13}$ cm^{-2} (Section 5.2), the HC_7N abundance in TMC-1 is $\sim 1 \times 10^{-9}$, similar to L1544.

Therefore, based on the simple estimates of the $n \geqslant 5$ cyanopolyyne abundances of TMC-1 and L1544, we confirm the general affirmation that the cyanopolyyne chemistry only depends on the gaseous carbon abundance. In other words, the $n \geqslant 5$ cyanopolyyne abundance ratios are the same regardless of the cause of the presence of gaseous carbon atoms. On the other hand, the $n \geqslant 5$ cyanopolyyne column density is a proxy of the cause of the gaseous carbon. For example, a column density of $HC_7N \sim 8 \times 10^{12}$ cm^{-2} would be a strong indication of a UV-illuminated gas.

6. Summary and Conclusions

We performed new observations using the GBT toward the prestellar core L1544. We detected several emission lines from cyanopolyynes from HC_3N to HC_9N, detected for the first time toward the source. The resolved spectral profiles show a double-peak profile, suggesting that the bulk of the cyanopolyyne emission is associated with the southern region of the core, where other smaller carbon chains peak. This supports the idea that cyanopolyynes are mainly formed in the external part

of the core, where the interstellar field radiation increases the free carbon atoms available to form long chains. We perform an LVG analysis of the observed HC_5N, HC_7N, and HC_9N lines, thanks to a new estimation of the collisional coefficients. The simultaneous fitting of the species indicates a gas kinetic temperature of 5–12 K, a source size of 80″, and a gas density larger than 100 cm^{-3}. The $HC_5N/HC_7N/HC_9N$ abundance ratios measured in L1544 are about 1/6/4. The measured column densities are lower by a factor 2–5 than those measured in TMC-1. Even if the measurements in other star-forming regions are scarce, the results obtained in L1544 suggest that a complex C-chain chemistry is active in other sources and is related to the presence of free gaseous carbon. The latter can be abundant either because the core is very young and the conversion to CO is not completed or because the CO is destroyed by UV illumination or cosmic-ray irradiation. We suggest that the column density of heavy cyanopolyynes (larger than HC_5N) could be a proxy to discriminate between these two regimes.

We are grateful to José Cernicharo for valuable discussions and suggestions. We thank the anonymous referee for the constructive comments. This project has received funding from (1) the European Research Council (ERC) under the European Union's Horizon 2020 research and innovation program, for the Project "The Dawn of Organic Chemistry" (DOC), grant agreement No 741002; (2) the PRIN-INAF 2016 The Cradle of Life—GENESIS-SKA (General Conditions in Early Planetary Systems for the rise of life with SKA); (3) the European Union's Horizon 2020 research and innovation programs under projects "Astro-Chemistry Origins" (ACO), grant No. 811312; and (4) the Deutsche Forschungsgemeinschaft (DFG, German Research Foundation) under Germany´s Excellence Strategy – EXC 2094 – 390783311. The Green Bank Observatory is a facility of the National Science Foundation operated under cooperative agreement by Associated Universities, Inc.

Facility: GBT.

Software: astropy (Astropy Collaboration et al. 2013, 2018), matplotlib (Hunter 2007).

ORCID iDs

Eleonora Bianchi https://orcid.org/0000-0001-9249-7082
Anthony Remijan https://orcid.org/0000-0001-9479-9287
Claudio Codella https://orcid.org/0000-0003-1514-3074
Cecilia Ceccarelli https://orcid.org/0000-0001-9664-6292
Francois Lique https://orcid.org/0000-0002-0664-2536
Silvia Spezzano https://orcid.org/0000-0002-6787-5245
Nadia Balucani https://orcid.org/0000-0001-5121-5683
Paola Caselli https://orcid.org/0000-0003-1481-7911
Eric Herbst https://orcid.org/0000-0002-4649-2536
Linda Podio https://orcid.org/0000-0003-2733-5372
Charlotte Vastel https://orcid.org/0000-0001-8211-6469
Brett McGuire https://orcid.org/0000-0003-1254-4817

References

Agúndez, M., & Wakelam, V. 2013, ChRv, 113, 8710
André, P., Men'shchikov, A., Bontemps, S., et al. 2010, A&A, 518, L102
Astropy Collaboration, Price-Whelan, A. M., Sipőcz, B. M., et al. 2018, AJ, 156, 123
Astropy Collaboration, Robitaille, T. P., Tollerud, E. J., et al. 2013, A&A, 558, A33
Ben Abdallah, D., Najar, F., Jaidane, N., Dumouchel, F., & Lique, F. 2012, MNRAS, 419, 2441
Berteloite, C., Le Picard, S. D., Balucani, N., Canosa, A., & Sims, I. R. 2010, PCCP, 12, 3677
Bizzocchi, L., Caselli, P., Spezzano, S., & Leonardo, E. 2014, A&A, 569, A27
Bockelée-Morvan, D., Lis, D. C., Wink, J. E., et al. 2000, A&A, 353, 1101
Burkhardt, A. M., Herbst, E., Kalenskii, S. V., et al. 2018, MNRAS, 474, 5068
Cabezas, C., Agúndez, M., Marcelino, N., et al. 2022, A&A, 659, L8
Caselli, P., Bizzocchi, L., Keto, E., et al. 2017, A&A, 603, L1
Caselli, P., & Ceccarelli, C. 2012, A&ARv, 20, 56
Caselli, P., Pineda, J. E., Sipilä, O., et al. 2022, ApJ, 929, 13
Caselli, P., Walmsley, C. M., Tafalla, M., Dore, L., & Myers, P. C. 1999, ApJL, 523, L165
Caselli, P., Walmsley, C. M., Zucconi, A., et al. 2002, ApJ, 565, 331
Ceccarelli, C., Caselli, P., Herbst, E., Tielens, A. G. G. M., & Caux, E. 2007, in Protostars and Planets V, ed. V. B. Reipurth, D. Jewitt, & K. Keil (Tucson: Univ. Arizona Press), 47
Ceccarelli, C., Codella, C., Balucani, N., et al. 2022, arXiv:2206.13270
Ceccarelli, C., Maret, S., Tielens, A. G. G. M., Castets, A., & Caux, E. 2003, A&A, 410, 587
Cernicharo, J., Bachiller, R., & Duvert, G. 1986, A&A, 160, 181
Cernicharo, J., Cabezas, C., Agúndez, M., et al. 2021, in Int. Symp. on Molecular Spectroscopy, A Sensitive Line Survey of TMC-1: The Chemical Complexity of a Cold Dark Cloud, doi:10.15278/isms.2021.TJ05
Cernicharo, J., Marcelino, N., Agúndez, M., et al. 2020, A&A, 642, L8
Chapillon, E., Dutrey, A., Guilloteau, S., et al. 2012, ApJ, 756, 58
Cordiner, M. A., Charnley, S. B., Buckle, J. V., Walsh, C., & Millar, T. J. 2011, ApJL, 730, L18
Cordiner, M. A., Charnley, S. B., Wirström, E. S., & Smith, R. G. 2012, ApJ, 744, 131
Crapsi, A., Caselli, P., Walmsley, M. C., & Tafalla, M. 2007, A&A, 470, 221
de Zafra, R. L. 1971, ApJ, 170, 165
Fournier, M. 2014, PhD thesis, http://www.theses.fr/2014REN1S100
Friesen, R. K., Medeiros, L., Schnee, S., et al. 2013, MNRAS, 436, 1513
Fuente, A., Navarro, D. G., Caselli, P., et al. 2019, A&A, 624, A105
Fukuzawa, K., Osamura, Y., & Schaefer, H. F., I. 1998, ApJ, 505, 278
Galli, P. A. B., Loinard, L., Bouy, H., et al. 2019, A&A, 630, A137
Giers, K., Spezzano, S., Alves, F., et al. 2022, A&A, 664, A119
Giesen, T. F., Harding, M. E., Gauss, J., Grabow, J.-U., & Muller, H. S. P. 2020, JMoSp, 371, 111303
Gupta, H., Gottlieb, C. A., McCarthy, M. C., & Thaddeus, P. 2009, ApJ, 691, 1494
Herbst, E., & Leung, C. M. 1989, ApJS, 69, 271
Hily-Blant, P., Faure, A., Vastel, C., et al. 2018, MNRAS, 480, 1174
Hirota, T., & Yamamoto, S. 2006, ApJ, 646, 258
Hollenbach, D. J., & Tielens, A. G. G. M. 1997, ARA&A, 35, 179
Hunter, J. D. 2007, CSE, 9, 90
Jaber Al-Edhari, A., Ceccarelli, C., Kahane, C., et al. 2017, A&A, 597, A40
Jiménez-Serra, I., Vasyunin, A. I., Caselli, P., et al. 2016, ApJL, 830, L6
Juvela, M. 2020, A&A, 644, A151
Keto, E., & Caselli, P. 2010, MNRAS, 402, 1625
Li, J., Shen, Z.-Q., Wang, J., et al. 2016, ApJ, 824, 136
Liu, X., Wu, Y., Zhang, C., et al. 2022, A&A, 658, A140
Loison, J.-C., Wakelam, V., Hickson, K. M., Bergeat, A., & Mereau, R. 2014, MNRAS, 437, 930
Loomis, R. A., Burkhardt, A. M., Shingledecker, C. N., et al. 2021, NatAs, 5, 188
Loomis, R. A., Shingledecker, C. N., Langston, G., et al. 2016, MNRAS, 463, 4175
Mauersberger, R., Henkel, C., & Sage, L. J. 1990, A&A, 236, 63
McCarthy, M. C., Levine, E. S., Apponi, A. J., & Thaddeus, P. 2000, JMoSp, 203, 75
McGuire, B. A., Burkhardt, A. M., Loomis, R. A., et al. 2020, ApJL, 900, L10
Müller, H. S. P., Schlöder, F., Stutzki, J., & Winnewisser, G. 2005, JMoSt, 742, 215
Müller, H. S. P., Thorwirth, S., Roth, D. A., & Winnewisser, G. 2001, A&A, 370, L49
Mumma, M. J., & Charnley, S. B. 2011, ARA&A, 49, 471
Punanova, A., Caselli, P., Feng, S., et al. 2018, ApJ, 855, 112
Quénard, D., Vastel, C., Ceccarelli, C., et al. 2017, MNRAS, 470, 3194
Ruffle, D. P., Hartquist, T. W., Caselli, P., & Williams, D. A. 1999, MNRAS, 306, 691
Sakai, N., Sakai, T., Hirota, T., Burton, M., & Yamamoto, S. 2009, ApJ, 697, 769

Sakai, N., Sakai, T., Hirota, T., & Yamamoto, S. 2008, ApJ, 672, 371
Sakai, N., Shiino, T., Hirota, T., Sakai, T., & Yamamoto, S. 2010, ApJL, 718, L49
Scoville, N. Z., & Solomon, P. M. 1974, ApJL, 187, L67
Snell, R. L., Schloerb, F. P., Young, J. S., Hjalmarson, A., & Friberg, P. 1981, ApJ, 244, 45
Snow, T. P., & McCall, B. J. 2006, ARA&A, 44, 367
Spezzano, S., Bizzocchi, L., Caselli, P., Harju, J., & Brunken, S. 2016, A&A, 592, L11
Spezzano, S., Caselli, P., Bizzocchi, L., Giuliano, B. M., & Lattanzi, V. 2017, A&A, 606, A82
Tafalla, M., Mardones, D., Myers, P. C., et al. 1998, ApJ, 504, 900
Urso, R. G., Palumbo, M. E., Ceccarelli, C., et al. 2019, A&A, 628, A72
Vastel, C., Ceccarelli, C., Lefloch, B., & Bachiller, R. 2014, ApJL, 795, L2
Vastel, C., Ceccarelli, C., Lefloch, B., & Bachiller, R. 2016, A&A, 591, L2
Walmsley, C. M., Winnewisser, G., & Toelle, F. 1980, A&A, 81, 245
Wernli, M., Wiesenfeld, L., Faure, A., & Valiron, P. 2007, A&A, 464, 1147
Wu, Y., Liu, X., Chen, X., et al. 2019, MNRAS, 488, 495